Journal of Materials Chemistry C

PAPER

Shape-dependent magnetism of bimetallic FeNi nanosystems

Cite this: J. Mater. Chem. C, 2014, 2, 6370

Nafiseh Moghimi, Fatemeh Rahnemaye Rahsepar, Saurabh Srivastava, Nina Heinig and Kam Tong Leung*

Shape-dependent magnetic properties of a bimetallic system have been studied for FeNi nanoparticles with well-defined concave cubic and octahedron shapes. The alloy composition was chosen to be close to that of an Invar FeNi alloy (with 35% Ni content) but with the coexistence of both bcc and fcc phases, in order to investigate the role of phase combinations in controlling the magnetic properties for the first time. Different saturation magnetization and coercivities were observed for the resulting FeNi alloy nanoparticles, and these differences have been correlated with surface anisotropy and formation of different two-phase combinations. The role of two-phase combinations in governing the magnetic properties has also been studied for both bulk and nanoalloys by large-scale Density Function Theory (DFT) calculations using VASP, which provides a new complementary approach to understanding the magnetic properties of alloy materials.

Received 6th March 2014
Accepted 30th May 2014

DOI: 10.1039/c4tc00443d

www.rsc.org/MaterialsC

Introduction

Studying shape-dependent magnetic properties of nanoparticles (NPs) offers rich insights into the fundamentals of magnetism in the nanoscale regime. As an important benchmark bimetallic magnetic system, the FeNi alloy system has been the subject of several theoretical and experimental investigations. This system is particularly intriguing because FeNi alloys such as Invar, Elinvar, and Permalloy exhibit notably different properties depending on their compositions. These alloys are not just interesting to basic research, but they also provide important practical applications. The phase diagram of a FeNi alloy exhibits three distinct regions (bcc, fcc, and bcc + fcc), which also make them a fascinating bimetallic material system for experimental and theoretical studies from the crystallography perspective. At room temperature, the coexistence of the bcc and fcc phases are observed when the Ni content is between 5% and 72%,[1] the range of which appears to depend on the method of preparation. For instance, the two-phase coexistence is found to occur at 15–34% Ni for alloys obtained by ball milling,[2] while thermal evaporation[3] and sputtering[4] produce alloys with a narrower %Ni range. Interestingly, this range is found to be wider when the size of the alloy is in the nanoscale regime.[5–7]

Magnetic properties of FeNi alloys as a function of composition has been studied over the entire range in both bulk and nanoalloys.[2–11] In most of the studies reported to date, the FeNi alloy has been found to exhibit a single-crystalline phase for each composition, *i.e.* either bcc or fcc. In few studies[2–4,9,11] when the alloy was obtained in the mixed-phase region, the percentage of each phase was not reported, which suggests that its importance has likely not been realized. For both bulk and nanosize, magnetic properties for FeNi alloys with a specific composition but a different combination of bcc and fcc phases are yet to be reported. In practice, when two phases coexist, the relative amount/percentage so obtained appears also to depend on the preparation method. Indeed, there is an acute need for studies on the role of different two-phase combinations in their magnetic properties. These studies are obviously very challenging to theory and experiment, because it has not been possible to make alloys with the same composition but with different two-phase combinations using a single method until now. By taking advantage of the unique nanoscale properties, we synthesize here $Fe_{63}Ni_{37}$ alloy NPs with two distinct shapes (but with the same composition), for which the combination of fcc and bcc phases in the mixed-phase region is different. This shape-dependent effect potentially provides a new control over the properties of an alloy with a specific composition. The *in situ* oxide nano-shell that covers the surface of NPs[5] will protect them against oxidation. We also provide the first investigation of the role of two-phase combinations in governing the magnetic properties in both bulk and nanoalloys by large-scale Density Function Theory (DFT) calculations.

Another important point to be noted here is that although there have been a few studies on shape-dependent magnetic properties of pure oxide nanoparticles of single metals (*e.g.* magnetites and ferrites),[12,13] there is no report on shape-dependent magnetic properties of bimetallic materials, including FeNi alloys or other transition metal combinations.

Department of Chemistry, University of Waterloo, Waterloo, Ontario, Canada N2L3G1. E-mail: tong@uwaterloo.ca

This is because of the challenges in the synthesis of bimetallic NPs with different shapes due to their inherent reactivities and easy oxidation. This work therefore provides the first experimental study of different magnetic properties of FeNi alloy NPs with different shapes.

Results and discussion

Concave cube (CC) and cuboctahedron (COh) NPs were prepared by co-electrodeposition of Fe and Ni on a H-terminated Si(100) substrate in a three-electrode cell by potentiostatic amperometry at −1.4 V *vs.* Ag/AgCl. A silicon chip (15 × 2.5 mm^2, 0.4 mm thick), precut from a Si(100) wafer (p-type, B-doped, with a resistivity of 0.01–0.02 Ω cm), was used as the working electrode, after it has been cleaned by using the RCA method[14] and further H-terminated by dipping in an aqueous HF (2%) solution. A standard Ag/AgCl electrode was used as the reference electrode while a Pt wire was used as the counter electrode. For CC NPs, we used an electrolyte solution consisted of 5 mM $FeCl_2$ and 5 mM $NiCl_2$ in 200 mM H_3BO_3 (used as the supporting electrolyte) and carried out the electrodeposition at room temperature. For COh NPs, electrodeposition was performed at 4 °C in a solution of 2.5 mM $FeCl_2$ and 1.25 mM $NiCl_2$ in 100 mM H_3BO_3 and 50 mM $NaClO_4$ (the latter two were used as the supporting electrolytes). Electrodeposition was carried out for 20 s and 30 s to obtain, respectively, the CC and COh NPs (with average sizes of 75 and 70 nm, respectively) shown in Fig. 1. The indentation (and the concavity) in the CC NPs indicates that the surfaces of the NPs are made up of high-index planes discussed in more detail elsewhere.[15] The corresponding alloy composition for both CC and COh NPs, as determined by Energy-Dispersive X-ray (EDX) analysis (to ±1% accuracy), is found to be $Fe_{63}Ni_{37}$, which is confirmed by lattice parameter measurements using X-ray Diffraction (XRD).[16] Glancing-incidence XRD patterns of both CC NPs and COh NPs shown in Fig. 1c indicate alloy formation with mixed fcc and bcc phases. The respective phase percentages are obtained by peak-fitting the most intense fcc (111) and bcc (110) features, after appropriate normalization of the two patterns to the fitted areas of the respective bcc (110) features. The respective amounts of fcc and bcc phases are found to be 37% and 63% for CC NPs and 48% and 52% for COh NPs (Table 1). It should be noted that the average size in Table 1 corresponds to the average diameter for spherical NPs or to the average side length for cubic NPs obtained by using image processing software. The grain size corresponds to the size of a crystallite (or grain) as estimated from the full width at half maximum of the most intense XRD peak by using the Scherrer equation. Within the accuracy of our measurements, the lattice constants for the fcc and bcc phases are essentially the same for both shapes (2.862 Å for bcc for both CC and COh NPs, and 3.578 Å and 3.589 Å for fcc for CC and COh NPs, respectively).

To investigate the local magnetic moments of the CC and COh NPs, we employ high-resolution magnetic force microscopy (MFM), using probe tips with low moments (<400 Oe) to minimize the perturbation of the sample by the magnetic field from the tip. Fig. 2 shows the topographic and magnetic force gradient images of the as-prepared CC and COh NPs (*i.e.* without pre-magnetization before the experiments). Evidently, CC NPs exhibit alternating bright and dark contrast among adjacent NPs, while COh NPs show dark contrasts for most of the neighboring particles. This suggests a lower coercivity for a CC NP as its moment could flip more easily than a COh NP. It is important to emphasize that the observed difference in local magnetic properties is due to differences in the shape and in the relative amounts of fcc and bcc components and not to the

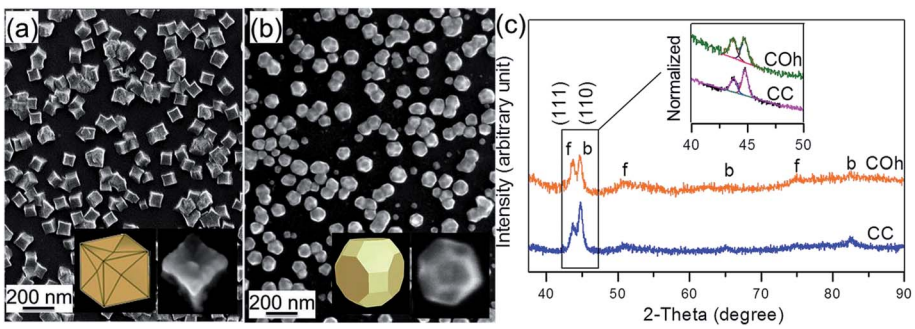

Fig. 1 SEM images of (a) concave cube (CC) and (b) cuboctahedron (COh) nanoparticles (NPs), with their corresponding higher magnification images and schematic diagrams shown in insets, and (c) glancing-incidence XRD patterns for CC and COh NPs. The peaks for the fcc and bcc phases are marked by "f" and "b", respectively, with the inset showing the most intense peaks for CC and COh NPs normalized to their respective bcc (110) peaks.

Table 1 Physical parameters of concave cube (CC) and cuboctahedron (COh) nanoparticles with the same composition of $Fe_{63}Ni_{37}$

$Fe_{63}Ni_{37}$ shape	Average size (nm)	Grain size (nm)	Lattice constant (Å)	bcc (%)	fcc (%)	Ms (emu g^{-1})	Coercivity (Oe)
CC	75 ± 1	35 ± 1	fcc: 3.578 bcc: 2.862	63	37	85	100
COh	70 ± 1	22 ± 1	fcc: 3.589 bcc: 2.862	52	48	40	188

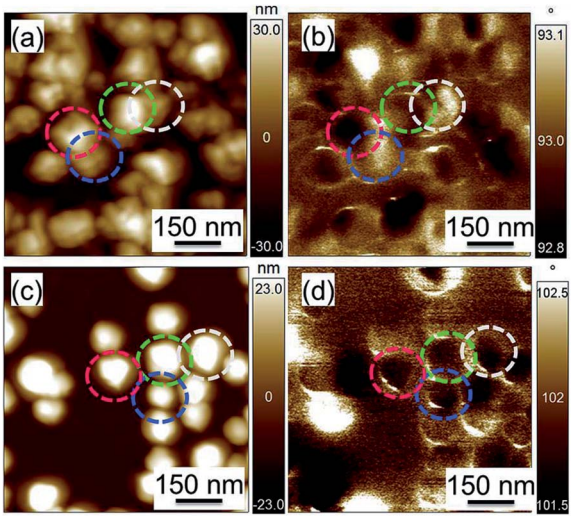

Fig. 2 Topographic (left) and magnetic force images (right) of (a) and (b) concave cubic (CC) and (c) and (d) cuboctahedron (COh) $Fe_{63}Ni_{37}$ nanoparticles collected at room temperature.

relative composition of Fe and Ni as the latter is the same ($Fe_{63}Ni_{37}$) for both CC and COh NPs.

In Fig. 3a, we compare the corresponding hysteresis loops for the $Fe_{63}Ni_{37}$ CC and COh NPs. A notably higher maximum

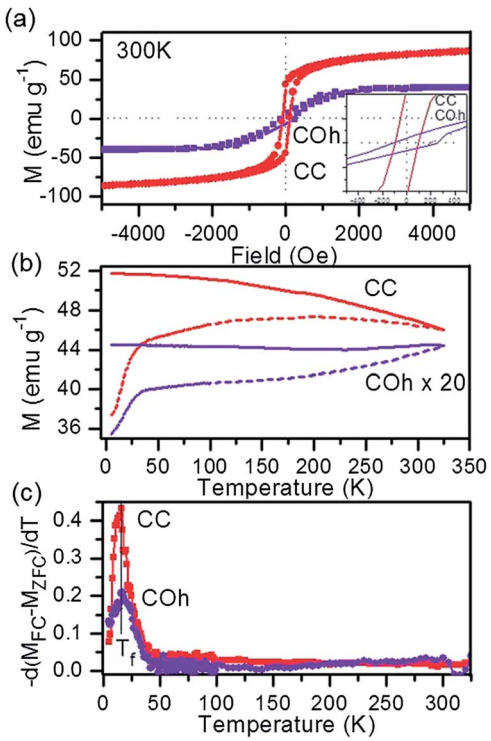

Fig. 3 (a) Hysteresis loops obtained at room temperature for both concave cube (CC) and cuboctahedron (COh) nanoparticles, with an expanded view over the −500 to 500 Oe range shown in the inset, (b) zero-field cooled (ZFC, dashed lines) and field-cooled (FC, solid lines) magnetization (M) curves in the presence of 100 Oe external field, (c) temperature derivative curves of the difference between FC and ZFC moments as functions of temperature.

magnetization at 0.5 T is found for the CC NPs (85 emu g^{-1}) than the magnetic saturation for COh NPs (40 emu g^{-1}), while the coercivity for the CC NPs (100 Oe) is smaller than that for the COh NPs (188 Oe) (Table 1), as expected from our MFM results. From Fig. 3a, it is clear that the magnetization of the CC sample is not saturating at the maximum applied field (0.5 T) at 300 K. This residual amount of unsaturation and a well-defined coercivity suggest the presence of a mixed phase of both ferromagnetism and superparamagnetism in the NPs. The maximum magnetization value for CC NPs is smaller than that reported for bulk $Fe_{63}Ni_{37}$ alloys[8–10,17,18] but is comparable to those found for FeNi alloy NPs reported previously.[19,20] The M_S value for COh NPs observed here is therefore lower than the FeNi NPs (with the same composition).[19,20] In order to compare with the previous work and with our own VASP calculations (discussed below), we estimate the moment per atom, μ, using the equation: $\mu = (M_{VSM} \times W)/(\mu_B \times N_A \times m)$, where M_{VSM} is the saturated magnetic moment or maximum magnetic moment obtained from VSM measurement, W is the molecular weight, μ_B is the Bohr magneton, N_A is the Avogadro number, and m is the mass of the sample. We obtain μ to be 0.95 μB per atom for CC and 0.40 μB per atom for COh NPs.

The hysteresis loop of the CC sample is characterized by a relatively large value of the magnetic remanence (M_r) to M_{VSM} ratio (0.52) and a nearly steep reversal of magnetization while that of the COh sample is characterized by a small M_r/M_{VSM} value (0.15) and a gradual change of magnetization to saturation. The large M_r/M_{VSM} value for CC NPs indicates that the particles consist of randomly oriented equiaxial grains with cubic magnetocrystalline anisotropy.[21] On the other hand, the smaller M_r/M_{VSM} value (less than 0.5) found for the COh NPs indicates that the grains inside the particles have magnetostatic interactions.[21] The larger M_r/M_{VSM} value for CC NPs compared to COh NPs is related to the increasing shape/magnetocrystalline anisotropy of the synthesized NPs due to a larger number of atoms that results in more missing coordination atoms. This difference in the remanence and shape of the MH curves, which shows a different magnetic behaviour, is due to differences in the shape and in the relative amounts of fcc and bcc components, as also illustrated in their MFM results.

Fig. 3b shows the temperature dependence of the magnetization at an applied field of 100 Oe for the CC and COh NPs after undergoing zero-field-cooled (ZFC) and field-cooled (FC) processes between 5 K and 325 K. The COh NP signal is scaled up 20 times for better illustration. An irreversible magnetic behavior, indicative of a large thermal irreversibility, is observed for both CC and COh NPs in the entire temperature range. For CC NPs, the ZFC magnetization increases with increasing temperature rapidly in the 5–30 K range and more slowly in the 30–200 K range and then decreases by a small amount upon increasing the temperature to 325 K. The relatively sharp increase of ZFC magnetization found in 5–30 K could be due to some small grains inside the NPs with the blocking temperature falling in this temperature range.[22] On the other hand, increasing the temperature for COh NPs results in increasing ZFC magnetization over the entire temperature range (5–325 K) with the rapid change in the 5–30 K range. As no

obvious maximum is observed in the ZFC magnetization from Fig. 3b, the blocking temperature should be above 325 K in a field of 100 Oe in these samples. The decreasing tendency of the ZFC curve for CC NPs up to 325 K can be due to the presence of superparamagnetism and ferromagnetism phases in the NPs as has been observed in the magnetization curve (Fig. 3a). Since there is no obvious peak in the ZFC magnetization curves of COh NPs, these NPs exhibit typical ferromagnetic behavior without any blocking temperature below 300 K. To confirm this result and to obtain some qualitative information about the magnetic behavior of these NPs, we show the temperature derivative curves of the differences between FC and ZFC magnetizations for the CC and COh NPs (Fig. 3c). The trend for this derivative curve is the same as that for the temperature derivative of the remanent magnetization.[23] The peak observed at 17 K for both CC and COh NPs represents a low-temperature, frozen, disordered magnetic state. The presence of this magnetic state therefore confirms ferromagnetic behavior for both CC and COh NPs and is consistent with that found in other non-relaxing (quasi-static) ferromagnetic materials (including Fe/Fe oxide and Ni/Ni oxide NPs) reported elsewhere.[23,24]

To account for the notable differences in M_S and coercivity of CC and COh NPs, we consider three plausible contributing factors: (1) particle or grain size, (2) surface anisotropy in different shapes, and (3) ratio of the amounts of bcc to fcc phases. Previous studies have shown that the saturation magnetization is very sensitive to the size of the NPs[25,26] or the grain size in thin films, with larger particles or grains exhibiting higher saturation magnetization.[27,28] We therefore expect that the CC NPs with a slightly larger particle size and larger grain size should show larger saturation magnetization than COh NPs. Furthermore, missing coordinating atoms around surface metal cations could lead to surface magnetic disorder and pinning. The surface anisotropy becomes lower whenever the coordination symmetry of the surface metal cations is more similar to that of the metal cations in the core of the NP.[29] For ferrite NPs, the surface anisotropy has been reported to be much smaller in cubic nanocrystals than that in spheres. This is likely because the curved topology of spherical nanocrystals could lead to more surface metal cations with less symmetric coordination and to more missing coordinating atoms than the flat surfaces of cubic nanocrystals.[12] Since these missing coordinating atoms and the surface anisotropy can change the coercivity,[30–32] the coercivity should follow the order: cube < octahedron cube < concave cube < sphere. Although both the concave cube and octahedron may have the same number of facets, the number of atoms is higher on the surface of the concave cube because of its higher index facets with more missing coordinating atoms. However, the saturation magnetization and remanent magnetization are independent of the surface anisotropy, as previously reported for $CoFe_2O_4$ and γ-Fe_2O_3 NPs with different shapes.[12,33] Furthermore, in the size range of our NPs (*i.e.* 70–75 nm), the surface atoms only represent less than 10% of the total number of atoms. Surface anisotropy therefore cannot account for the observed difference in M_S for CC and COh NPs.

To evaluate the role of the ratio of the amounts of bcc to fcc phases on the magnetic behavior of NPs, we perform Density Function Theory (DFT) calculation[34] using the Vienna *Ab initio* Simulation Package (VASP, Version 5.2)[35] with the MedeA platform (Materials Design). According to the lattice parameters, the fcc phase has a chemical composition close to that of the alloy itself. The bcc phase must also have nearly the same composition as the alloy according to the previous X-ray lattice parameter measurements on alloys with similar chemical compositions of bcc and fcc phases.[36,37] We therefore construct bcc lattices with super-cells of 256 atoms for the ordered structure and of 108 atoms for the disordered structure, all with the closest composition to $Fe_{63}Ni_{37}$ composition (where X and Y in the Fe_XNi_Y notation correspond to atom% and not the actual numbers of atoms of Fe and Ni, respectively). For fcc lattices, super-cells of 128 atoms for both ordered and disordered structures are used. The ordered structures are obtained by repeating smaller unit cells to construct the super-cell. For example, the super-cell of 256 atoms for bcc is made up of Fe5Ni3 unit cells (where *A* and *B* in the FeANiB notation correspond to the numbers of Fe and Ni atoms, respectively, in the small cell), while the super-cell of 108 atoms for fcc is made up of Fe11Ni7 unit cells. For disordered structures, the atoms are randomly placed in the structure, and the respective super-cell does not contain any repeating structure inside and therefore no smaller unit cells. For example, the super-cell of 108 atoms for the disordered fcc structure is made up of Fe67Ni41. Furthermore, we have also tested several other different initial disordered arrangements and obtained their optimized disordered structures, the cohesive energies of which are found to be similar. This result is also consistent with our observation using super-cells containing the same number of atoms (*e.g.* 128) but in different volumes for the disordered structures. Our objective here is to use the results obtained for these single-phase crystalline super-cells (*i.e.* bcc or fcc) to deduce the properties of the NPs with two-phase combinations. We employ the projector-augmented wave (PAW) method and the exchange correlation with the generalized gradient approximation by the Perdew, Burke, and Ernzerhof (PBE-GGA)[38] for structure optimization and magnetic moment calculation (assuming the periodic boundary conditions). The wave-functions are expanded in a plane wave basis with energy cutoffs of 267.88 eV for Fe and of 269.53 eV for Ni. The surface Brillouin zone was sampled at the Γ point with a k-point spacing of 0.5 $Å^{-1}$. The geometries have been optimized by relaxing all atoms until the forces are less than 20 meV $Å^{-1}$, with the energy convergence of the self-consistent-field set to 1.0×10^{-3} eV and Methfessel–Paxton smearing set to 0.2 eV, while keeping the cell constants for the crystal fixed. Since structure optimization by relaxing the lattice parameters has been found to change the original crystal structure (phase and symmetry), we have therefore not included lattice parameter relaxation in the optimization. Given that we constructed super-cells using the pre-defined crystal structures in VASP, the appropriate periodic boundary conditions have been used during structure optimization. The spin-orbit combined magnetic and Vosko–Wilk–Nusair spin-interpolation methods[39] have been employed for the total moment calculations.

The DFT calculations have produced optimized atomic arrangements in the bcc and fcc unit cells with ordered and disordered structures. According to the cohesive energies, the most stable configurations are (Fe11Ni7) × 6 and (Fe5Ni3) × 16 for the fcc and bcc ordered structures, respectively, and Fe67Ni41 and Fe79Ni49 for the respective fcc and bcc disordered structures. In Fig. 4a, we summarize the calculated cohesive energies of these super-cells along with their optimized structures, which indicate their relative ease of formation. From the total moments calculated for the optimized super-cell structures, we estimate the moment per atom for each structure. As an independent check of the VASP accuracy, we obtain, in separate calculations, the magnetic moments of a pristine Fe and a pristine Ni super-cells, and compare these values [2.2 μB per atom for Fe and 0.6 μB per atom for Ni] with the respective experimental moments for these elements reported in the literature.[8,11] Excellent agreement is found for both Fe and Ni, confirming the high accuracy of our VASP calculations. We also compare the VASP results for the single-phase fcc and bcc $Fe_{63}Ni_{37}$ super-cells in ordered and disordered structures with the experimental values obtained for bulk alloys reported in the literature.[18,40,41] Fig. 4b shows the literature experimental M_S values obtained for fcc and bcc alloys in the region of an Invar alloy (*i.e.* 30–38 Ni%) and the calculated magnetic moments for ordered and disordered bcc and fcc unit cells by VASP. In Fig. 4b, the upper horizontal line and the lower horizontal line mark the moments for ordered bcc and disordered fcc, respectively, which correspond to the more stable configurations with less positive cohesive energies for the bcc and fcc lattices (shown in Fig. 4a). Evidently, the VASP results are very close to the experimental literature values. It should, however, be noted that the amounts of fcc and bcc phases are not indicated in the previous reports, and as explained below this information is important because it could account for the observed discrepancy. By combining different percentages of bcc and fcc unit cells, we could obtain the total magnetic moment of the two-phase structure over the entire range from pure bcc phase to pure fcc phase. Fig. 4c shows that the calculated total magnetic moment could vary from 1.87 μB per atom for the pure bcc phase to 1.15 μB per atom for the pure fcc phase. This therefore confirms that the total magnetic moments obtained for alloys with two phases strongly depend on their phase combination. This is the first report on the role of phase combination on the magnetic moment of the alloy, which could be used to explain the differences in M_S values found for FeNi alloys with the same composition reported in the literature. For our case with the bcc-to-fcc combinations of 63% to 37% for CC NPs and of 52% to 48% for COh NPs, this difference (0.1 μB per atom, Fig. 4c) is found to be quite significant. It should be noted this difference is also expected to be larger in the nano-regime because of the larger defect sites, boundary effects and surface effects.

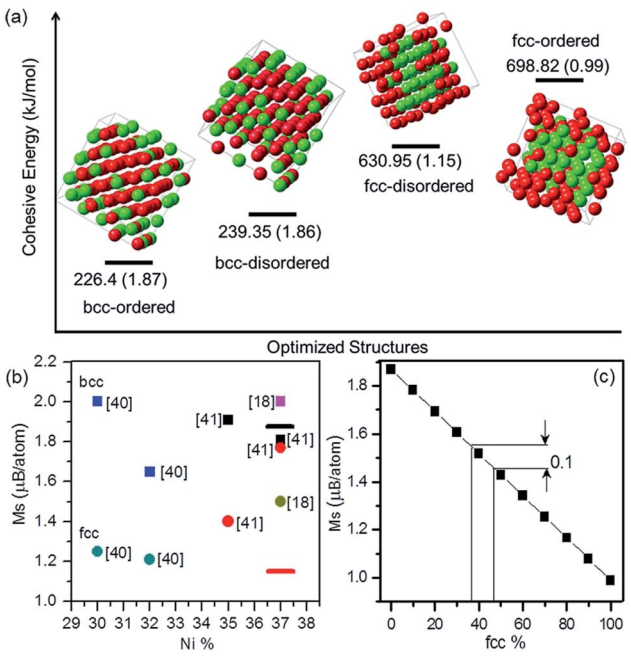

Fig. 4 (a) Optimized ordered and disordered structures and the corresponding cohesive energies (in units of kJ mol^{-1}, not drawn to scale) and total moments (in parentheses, and in units of μB per atom) for the most stable $Fe_{63}Ni_{37}$ super cells and (b) comparison of experimental magnetic saturation M_S obtained for bcc (squares) and fcc unit cells (circles) for bulk alloys [ref. 18, 40 and 41] with the VASP results (upper horizontal line for bcc and lower horizontal line for fcc). (c) variation of total moment as a function of fcc unit cells in different combinations of bcc to fcc phases.

In conclusion, the magnetic properties of well-defined concave cubic and cuboctahedron nanoparticles with the same composition but different shapes and two-phase combinations have been investigated by detailed magnetization experiments and VASP calculations. We show that these NPs with the specific shapes and two-phase combinations but the same composition could be easily produced on Si(100) by electrochemical deposition using appropriate electrolytes. The saturation magnetization and coercivity are found to be different for CC and COh NPs, and these differences have been correlated with the surface anisotropy and different two-phase combinations of bcc and fcc phases inside the nanoparticles. Large-scale VASP computational study of the role of different two-phase combinations for a particular composition of FeNi alloys has also been carried out. These calculations offer new insights into magnetic properties of both bulk and nanoalloys consisting of two crystalline phases and can be used to explain the observed differences. In addition to the particle shape, the two-phase combination could therefore provide an important parameter and must be considered in further controlling the magnetic properties of bimetallic alloy nanoparticles.

Acknowledgements

This work was supported by the Natural Sciences and Engineering Research Council of Canada. N. Moghimi gratefully acknowledges the support of a WIN Fellowship. We are grateful to Dr Jason Li (Asylum Inc.) for assistance with the AFM experiments and to Dr Shantinarayan Routi for helpful discussion.

References

1 X. Wei, G. Zhu, J. Zhou and H. Sun, *Mater. Chem. Phys.*, 2006, **100**, 481–485.
2 L. B. Hong and B. Fultz, *J. Appl. Phys.*, 1996, **79**, 3946.
3 G. Dumpich, E. F. Wassermann, V. Manns, W. Keune, S. Murayama and Y. Miyako, *J. Magn. Magn. Mater.*, 1987, **67**, 55–64.
4 Y. Sumiyama, K. Kadono and M. Nakamura, *Trans. Jpn. Inst. Met.*, 1983, **24**, 190–194.
5 N. Moghimi, S. Bazargan, D. Pradhan and K. T. Leung, *J. Phys. Chem. C*, 2013, **117**, 4852–4858.
6 L. H. Zhu, X. M. Ma and L. Zhao, *J. Mater. Sci.*, 2001, **36**, 5571–5574.
7 H. Wu, Y. Cao, P. Yuan, H. Xu and X. Wei, *Chem. Phys. Lett.*, 2005, **406**, 148–153.
8 M. F. Collins and J. B. Forsyth, *Philos. Mag.*, 1963, **8**, 401–410.
9 X. G. Li, A. Chiba and S. Takahashi, *J. Magn. Magn. Mater.*, 1997, **170**, 339–345.
10 M. F. Collins, R. V. Jones and R. D. Lowde, *J. Phys. Soc. Jpn.*, 1962, **17**, 19–26.
11 B. Glaubitz, S. Buschhorn, F. Brüssing, R. Abrudan and H. Zabel, *J. Phys.: Condens. Matter*, 2011, **23**, 254210.
12 Q. Song and Z. J. Zhang, *J. Am. Chem. Soc.*, 2004, **126**, 6164–6168.
13 G. Gao, X. Liu, R. Shi, K. Zhou, Y. Shi, R. Ma, E. Takayama-Muromachi and G. Qiu, *Cryst. Growth Des.*, 2010, **10**, 2888–2894.
14 W. Kern, *Handbook of Semiconductor Wafer Cleaning Technology*, NJ, 1993.
15 N. Moghimi, M. Abdellah, J. P. Thomas, M. Mohapatra and K. T. Leung, *J. Am. Chem. Soc.*, 2013, **135**, 10958–61.
16 A. J. Bradley, *Philos. Mag.*, 1937, **23**, 545–557.
17 F. Hegg, *Arch. Sci. Phys. Nat.*, 1910, **4**, 592–617.
18 P. James, O. Eriksson, B. Johansson and I. Abrikosov, *Phys. Rev. B: Condens. Matter Mater. Phys.*, 1999, **59**, 419–430.
19 X. L. Dong, Z. D. Zhang, X. G. Zhao and Y. C. Chuang, *J. Mater. Res.*, 1999, **109**, 7203–7207.
20 M. H. Xu, W. Zhong, X. S. Qi, C. T. Au, Y. Deng and Y. W. Du, *J. Alloys Compd.*, 2010, **495**, 200–204.
21 *Nanoparticles and Nanostructured Films: Preparation, Characterization and Applications*, ed. J. H. Fendle, WILEY-VCH Verlag GmbH & Co. KGaA, NY, 1998.
22 Z. L. Wang, Y. Liu and Z. Zhang, *Handbook of Nanophase and Nanostructured Materials: Material Systems and Applications I*, Kluwer Academic, Boston, 2003.
23 L. Del Bianco, D. Fiorani, A. Testa, E. Bonetti, L. Savini and S. Signoretti, *Phys. Rev. B: Condens. Matter Mater. Phys.*, 2002, **66**, 174418.
24 M. Thakur, M. Patra, S. Majumdar and S. Giri, *J. Alloys Compd.*, 2009, **480**, 193–197.
25 C. H. Chia, S. Zakaria, M. Yusoff, S. C. Goh, C. Y. Haw, S. Ahmadi, N. M. Huang and H. N. Lim, *Ceram. Int.*, 2010, **36**, 605–609.
26 A. Demortière, P. Panissod, B. P. Pichon, G. Pourroy, D. Guillon, B. Donnio and S. Bégin-Colin, *Nanoscale*, 2011, **3**, 225–232.
27 K. W. Kim, K. S. Yoon, J. H. Koo, Y. H. Do, C. O. Kim and J. P. Hong, *IEEE Trans. Magn.*, 2006, **42**, 1495–1498.
28 Y. L. Soo, T. S. Wu, C. S. Wang, S. L. Chang, H. Y. Lee, P. P. Chu, C. Y. Chen, L. J. Chou, T. S. Chan, C. A. Hsieh, J. F. Lee, J. Kwo and M. Hong, *Appl. Phys. Lett.*, 2011, **98**, 031906.
29 C. R. Vestal and Z. J. Zhang, *J. Am. Chem. Soc.*, 2003, **125**, 9828–9833.
30 J. S. Miller and M. Drillon, *Magnetism: Molecules to Materials III*, John Wiley & Sons, Inc, 2002.
31 H.-L. Sun, H. Shi, F. Zhao, L. Qi and S. Gao, *Chem. Commun.*, 2005, 4339–4341.
32 A. Dimitrov and M. Wysin, *Phys. Rev. B: Condens. Matter Mater. Phys.*, 1994, **50**, 3077–3084.
33 G. Salazar-Alvarez, J. Qin, I. Bergmann, M. Vasilakaki, K. N. Trohidou, J. D. Ardisson, W. A. A. Macedo, M. Mikhaylova, M. Muhammed, M. D. Baro and J. Nogues, *J. Am. Chem. Soc.*, 2008, **130**, 13234–13239.
34 W. Kohn and L. J. Sham, *Phys. Rev.*, 1965, **140**, 1133–1138.
35 G. Kresse and J. Furthmuller, *Comput. Mater. Sci.*, 1996, **6**, 15–50.
36 J. Eckert, J. C. Holzer and W. L. Johnson, *J. Appl. Phys.*, 1993, **73**, 131–141.
37 J. Eckert, J. C. Holzer, C. E. Krill and W. L. Johnson, *J. Appl. Phys.*, 1993, **73**, 2794–2802.
38 J. Perdew, K. Burke and M. Ernzerhof, *Phys. Rev. Lett.*, 1996, **77**, 3865–3868.
39 S. H. Vosko, L. Wilk and M. Nusair, *Can. J. Phys.*, 1980, **58**, 1200–1211.
40 J. Crangle and G. C. Hallam, *Proc. R. Soc. London, Ser. A*, 1963, **272**, 119–132.
41 (*a*) E. J. Kondorsky and L. N. Fedotov, *Invest. Akad. Nauk., SSSR*, 1952, **16**, 432; (*b*) M. Peschard, *Rev. Met*, 1925, **22**, 490, 581, 663.